

Ripple formation over a sand bed submitted to a laminar shear flow

A. Valance^a and V. Langlois

Groupe Matière Condensée et Matériaux, UMR 6626, Université Rennes 1, 35042 Rennes Cedex, France

Received 2 September 2004 / Received in final form 3 December 2004

Published online 25 February 2005 – © EDP Sciences, Società Italiana di Fisica, Springer-Verlag 2005

Abstract. We investigate the process of ripple formation in a viscous fluid when a sand bed is submitted to a laminar shear flow. We propose a new description for the sand transport which takes into account the fact that the transport rate does not adapt instantaneously to a change of the fluid velocity due to grain inertia. It introduces a new length, called here after equilibrium length l_{eq} , corresponding to the distance needed for a immobile grain to equilibrate its velocity with that of the fluid. The transport rate is therefore found to depend not only on the fluid shear stress and bed slope (as usually assumed) but also on grain inertia. Within the framework of this model we analyzed the mechanisms of the sand bed instability. It is found that the instability results from the competition between the destabilizing effect of fluid inertia and the stabilizing ones of grain inertia and bed slope. We derive analytical scaling laws for the most amplified wavelength, its growth rate and phase velocity. We found in particular that at small particle Reynolds number Re_p , the most amplified wavelength scales as the viscous length l_ν defined as $\sqrt{\nu/\gamma}$ (where γ is the shear rate and ν the fluid viscosity) and at large Re_p it scales as the equilibrium length l_{eq} . Our results are compared with available experimental data.

PACS. 45.70.-n Granular systems – 47.15.-x Laminar flows – 47.54.+r Pattern selection; pattern formation

1 Introduction

When an initially flat sand bed is sheared by a fluid, the bed is unstable and gives rise to formation of ripples. This generic sand pattern results from a complex feedback mechanism between the flow and the bed form. At the first stages of the pattern formation, the bed develops a regular pattern of small-amplitude waves which further evolves toward an equilibrium bedform generally of much greater extent. Despite the huge number of experimental and theoretical studies about ripple formation, this problem is not well understood and even the physical origin of the instability mechanism is questioned. This is essentially due to the fact that there exists no well-established equations describing the coupling between the fluid and the bed form.

Several configurations have been investigated depending on the oscillatory or steady nature of the flow. Ripples observed in seas along beaches are an example corresponding to the oscillating case whereas those forming in rivers illustrate the steady configuration. Another important parameter is the flow depth. In shallow water, deformation of the upper fluid surface couples with the sand bed. This coupling becomes irrelevant when the flow depth is great enough.

The classical way of dealing with the problem of ripple formation is as follows. The deformation of the sand bed is generally assumed slow compared with the fluid velocity such that the flow over a slightly deformed bed is calculated as if it were fixed. The fluid shear stress at the bed surface is then derived and the corresponding grain transport rate is calculated using semi-empirical laws. The most commonly used law is that of Meyer-Peter [1] which reads:

$$q \propto \sigma_b^{3/2} \quad (1)$$

where q is the grain transport rate and σ_b the fluid shear stress at the sand bed surface. The growth rate of the bed modes is then deduced from mass conservation equation

$$\frac{\partial h}{\partial t} = -\frac{\partial q}{\partial x} \quad (2)$$

where h is the height of the sand bed and x is the spatial horizontal coordinate. The bed instability develops as soon as there is a positive phase lag between the bed profile and the transport rate. More precisely, if $h \sim e^{ikx+\omega t}$ and $q \sim h e^{i\psi(k)}$ (where k is the wavenumber of the profile perturbation, ω its growth rate, and ψ is the phase shift of the transport rate; the proportionality between h and q is justified within the framework of a linear analysis), the growth rate of the mode k is given by: $\omega = k[\sin \psi(k) - i \cos \psi(k)]$. The bed is unstable if there exists a

^a e-mail: alexandre.valance@univ-rennes1.fr

band of modes k for which the real part of the growth rate is positive, i.e., $\pi > \psi(k) > 0$. In other words, a mode k is unstable when the local transport rate reaches its maximum value just before the maximum of the bed height. As the transport rate is related to the flow shear stress at the bed, it also means that the latter is shifted upstream in comparison to the bed height profile.

The first theoretical works concerning the stability analysis of the fluid-bed interface [2–4] were based on potential flow models to describe the flow over the bed. Unfortunately, within these models, there is no phase lag between the local flow condition and the bed profile. In order to get an instability, most authors [2–4] put artificially by hands a phase lag for which it is difficult to associate appropriate values for flow systems. More recently, Fenton et al. [5] showed that potential flow models where an explicit phase lag is adopted results in predictions that are not consistent with observed flow systems. They reassessed these potential flow models without the use of explicit lag and by releasing the usual quasi-steadiness approximation. Instability is shown to occur via a resonance mechanism between surface waves and bed waves traveling at the same celerity. However, the prediction of the unstable wavelengths are not consistent with observations of physical flow systems. Fenton et al. conclude therefore that potential flow should no longer form the basis of the instability describing bed form generation from the flat bed condition.

Another approach is to use rotational flow models, as those developed by Richards [6], and Sumer and Bakioglu [7]. Within these models, the turbulent flow close to the bed is described via a height dependent eddy-viscosity approach. Two main results follow. (i) The turbulent flow shear stress appears to follow the bed perturbation with a phase lag which generates the bed instability, whereas gravitational force acts as a stabilizing mechanism at short wavelength (gravity impedes grain motion up stoss slopes and aids it down lee slope). (ii) Two separate unstable modes corresponding to formation of dunes (i.e., the large scale structure) and ripples (i.e., the small scale one) respectively are predicted. The first one is function of the roughness height y_0 of the bed, the effect of the local bed slope on bed load sediment transport (characterized by the intern angle ϕ_s of friction of the granular material) and the depth H of the flow. For the second mode of instability, $\lambda = 2\pi/k$ depends solely of ϕ_s and y_0 : $\lambda \sim f(\phi_s)y_0$ where f is a increasing function of ϕ_s . The parameter y_0 scales as a first approximation with the diameter d of the grain. Nikuradse [8] found a value of $y_0 = d/30$ for fixed bed made of single grain size. However, this value seems underestimated for erodible bed. Smith and Mc Lean [9] indeed showed that for flows over a mobile bed the moving sediment will affect the value of y_0 . The value generally adopted is $y_0 \simeq 4d$. Taking this value, the prediction of such turbulent models predicts an initial wavelength of the structure comparable with that of observed ripples in the experiments of Coleman and Melville [10] but it is much shorter than that observed in other experiments [11].

The first limitation of these turbulent flow models is the difficulty to associate appropriate values for y_0 which depends on intricate parameters (flow shear stress, height of the bed-load layer, grain diameter). Furthermore the effective roughness of the bed increases as the ripples grow. Second, the prediction of turbulent models seems very sensitive to the parametrisation used to model the turbulence.

A natural question arises: is the turbulence necessary to observe the formation of ripples? Recently Charru et al. [12] addressed this issue and showed theoretically that a viscous flow may be responsible for the bed instability. This prediction has been confirmed recently by Rabaud et al. [13] through a quasi-2D flow experiment. The case of a viscous flow presents the great advantage to be solved much more easily without approximation and offers deep insights into the instability mechanism. Charru et al., using a rate transport law similar to that of Meyer-Peter formula (Eq. (1)), found that for high fluid thickness, the flat bed is unstable as soon as the grains move and that the most dangerous wavelength scales with the viscous length $l_\nu = (\nu/\gamma)^{1/2}$, where ν is the fluid viscosity and γ the fluid shear rate. This results from the competition between the destabilizing effect of fluid inertia (which generates a lag between the flow shear stress and the bed perturbation) and the stabilizing one due to gravity already mentioned above. It is important to note that the lag is generated by the coupling between the fluid inertia and the viscous effects. An inviscid flow, or a Stokes flow, does not exhibit such a phase lag. Within this viscous flow model, the predicted most dangerous wavelength is still underestimated (by a factor of 10) in comparison with data furnished by available experiments [13].

We present in this article a new model describing the process of ripple formation in the case of a laminar shear flow. More precisely, our model takes into account the grain inertia in the evaluation of the sediment transport, which seems to play an important role in the selection of the most amplified unstable wavelength. Due to grain inertia, the flux of transported sediment does not equilibrate instantaneously with the fluid velocity. As a consequence, there exists a lag between the sediment transport and the fluid velocity. This lag introduces an additional stabilizing mechanism which affects the selection of the most dangerous mode. As to be seen further, this lag can be expressed in terms of a characteristic length, called hereafter ‘equilibrium length’, that is associated with the distance needed for an immobile grain to equilibrate its velocity with that of the fluid.

Within this model, we derive new analytical scaling laws for the most dangerous mode which is found to be a combination between the viscous length and the equilibrium length. Moreover, the estimation of the most dangerous wavelength, in the regimes where grain inertia is pertinent, seems to be in reasonable agreement with available experimental data.

We should emphasize that in the majority of experiments and natural conditions where ripple formation occurs, the flow is turbulent. Our analysis is not intended to describe those situations but rather to apply

to experiments carried out within quasi-2D flows (e.g., in Hele-Shaw cell), where flows are expected to remain laminar at large flow speed, as to be seen further. Although these limitations, such laminar analyses present yet some great interest because first, they provides us with analytical expressions for the wavelength, the growth rate and the drift velocity of the ripple pattern as a function the physical parameters of the problem (grain diameter, shear rate, fluid viscosity), and, second, they allow to clearly identify the influence of the physical mechanisms introduced in the model.

The article is organized as follows. In Section 2, we present the model equations and discuss the approximations used to solve them. The basic solution of the model corresponding to a flat sand bed is analyzed in Section 3, whereas Section 4 is devoted to the presentation of the linear stability analysis and its predictions about the growth rate and drift velocity of unstable modes. Finally, discussion and conclusion are presented in Section 5.

2 Model equations

We consider a laminar shear fluid flow over a deformed sand bed (see Fig. 1). The bed deformation is assumed to have dimensions small compared with the width L of the flow. The fluid is viscous and Newtonian, and the speed U_∞ at $y = L$ is fixed by the operator. Furthermore, we will restrict ourselves to a two-dimensional analysis. In other words, we assume that the bed deformation is invariant along the horizontal direction perpendicular to the fluid flow. We first briefly present the fluid motion equations together with the boundary conditions employed. Then we describe the model used for sediment transport.

2.1 Hydrodynamic equations

The motion equations of the fluid reads:

$$\rho_f \frac{\partial \mathbf{u}}{\partial t} + \rho_f (\mathbf{u} \cdot \nabla) \mathbf{u} = -\nabla p + \eta \nabla^2 \mathbf{u}, \quad (3)$$

$$\nabla \cdot \mathbf{u} = 0, \quad (4)$$

where $\mathbf{u} = (U, V)$ is the fluid velocity, ρ_f the fluid viscosity, η the dynamic fluid viscosity ($\eta = \rho_f \nu$, ν being the kinematic density) and p is the fluid pressure. The boundary conditions at the top surface (i.e., $y = L$) are given by:

$$U = U_\infty \text{ and } V = 0, \quad (5)$$

whereas at the sand bed surface one imposes the following conditions:

$$-\frac{\partial h}{\partial x} U + V = \frac{\partial h}{\partial t}, \quad (6)$$

$$U + \frac{\partial h}{\partial x} V = 0. \quad (7)$$

h measures the local height of the sand bed. Equation (6) expresses the fact that the fluid velocity normal to the bed

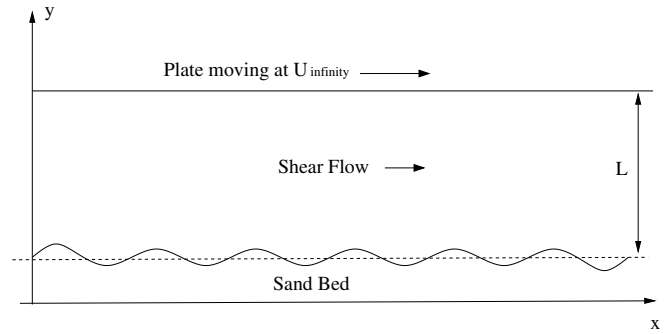


Fig. 1. Two-dimensional laminar shear flow over a deformed sand bed.

surface, v_n , is equal to the normal displacement speed of the bed surface, and equation (7) stands for the no-slip condition at the sand bed surface. The latter condition can be legitimately questioned since some grains of the top layer of the sand bed are moving. However, the condition used at the sand bed surface (zero or non-zero slip velocity) is not really crucial because, as to be seen below, it is the bed shear stress, which determines the transport rate.

2.2 Sediment transport and bed profile evolution

It is common to describe the sediment transport in viscous fluids (like water) in terms of two main transport modes: bed load and suspended load [1]. The bed load is defined as the part of the total load that is more or less in continuous contact with the bed during the transport. Thus the bed load is determined almost exclusively by the effective bed shear acting directly on the sand surface. The suspended load is the part of the total load that is moving without continuous contact with the bed. We choose to concentrate on the bed-load sediment and neglect the transport of suspended material. This is not a real short-coming as in the ripple formation process bed-load transport is usually dominant.

We will first present the classical model used to describe the sand transport and then introduce the changes needed to take into account grain inertia. Let us call $q(x, t)$ the vertically integrated volumetric sand flux. The sand flux is linked to the height $h(x, t)$ of the sand bed profile via the mass conservation equation:

$$\frac{\partial h}{\partial t} = -\frac{\partial q}{\partial x}. \quad (8)$$

The sand flux is usually taken to be equal to an ‘equilibrium’ value q_{eq} estimated from steady and fully developed regimes. A lot of semi-empirical expressions for the equilibrium sand flux have been proposed and have the following generic form [1]:

$$q_{eq} = q_b (\Theta - \Theta_c)^n, \quad (9)$$

where q_b is proportional to a volumetric sediment transport: $q_b = c\sqrt{(s-1)gd^3}$ (c being a numerical constant).

Θ denotes the Shields parameter defined by

$$\Theta = \frac{\sigma_b}{\rho_f g (s-1) d}, \quad (10)$$

where σ_b is the bed shear stress and $s = \rho_g/\rho_f$ is the relative density of the grains with respect to the fluid density. Θ_c is the critical Shields parameter above which sediment starts to move and depends on the bed slope. The dependence of Θ_c with the bed slope is usually modeled as follows [1]:

$$\begin{aligned} \Theta &= \Theta_{c0} \cos \phi \left(1 - \frac{\tan \phi}{\tan \phi_s} \right) \\ &= \frac{\Theta_{c0}}{\sqrt{1 + h_x^2}} \left(1 + \frac{h_x}{\tan \phi_s} \right), \quad (11) \end{aligned}$$

in which ϕ is the angle of the bed slope and Θ_{c0} indicates the critical Shields parameter on a bed with no slope. The parameter ϕ_s is the intern angle of friction of the granular material. There exist various estimates of the critical Shields parameter available in the literature [1,20]. The spectrum of the reported values (from 0.05 to 0.35) is quite large, reflecting the difficulty of defining this threshold with accuracy. Moreover, the threshold is expected to be extremely sensitive to the features of the grain packing in the sand bed (loose or close-packed arrangement). For our purpose, we will take an average value $\Theta_{c0} \approx 0.2$.

The laws used in the literature to model the sediment transport have the form of equation (9) with a definite value for the exponent n . In the Meyer-Peter law [1], $n = 3/2$ and $c = 8$, whereas Bagnold [21] proposed a sediment transport law with $n = 3$. We will see that the value of n is unimportant when one remains in the framework of a linear analysis of the sand bed profile evolution.

The standard approximation is to consider that the actual sand flux is equal to the equilibrium value: $q = q_{eq}$. That means that one implicitly assumes that the sand flux adapts instantaneously to a change of the fluid velocity. Here, one will consider that this is not the case due to grain inertia. Indeed, if the fluid velocity increases, it takes some time for the grains, initially at rest, to reach the fluid velocity. This characteristic equilibrium time can be associated with an equilibrium length l_{eq} , which corresponds the distance needed for grains, initially at rest, to equilibrate their velocity with that of the fluid. This concept of equilibrium length has been also introduced in the context of aeolian sand transport [14]. There exist different possible approaches to describe the evolution of the sand flux towards its equilibrium value q_{eq} . We will take, for sake of simplicity, a simple relaxation law, which can be written as

$$\frac{\partial q}{\partial x} = -\frac{q - q_{eq}}{l_{eq}}. \quad (12)$$

This equation is analog to that used in the context of aeolian sand transport [14–16]. It is also worth noting that this equation can be derived from a “BCRE-like” approach which quantifies the balance between the erosion and deposition processes [17,18].

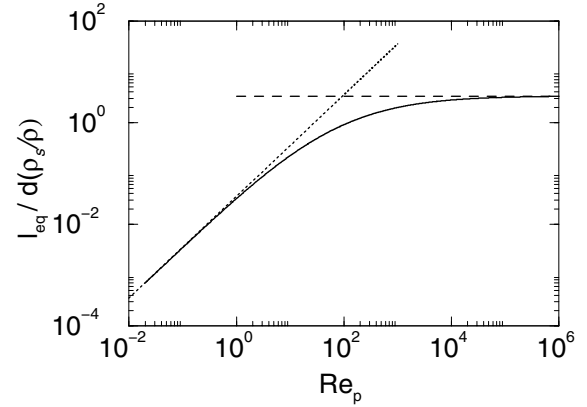


Fig. 2. Equilibrium length as a function of the particle Reynolds number. For $Re_p < 10$, $l_{eq} \sim Re_p d$ (dotted curve), whereas l_{eq} becomes independent of Re_p for large Re_p (dashed curve).

Equations (8) and (12) together with equation (9) constitute the evolution equations of our model. Finally, we should provide an estimation of the equilibrium length as a function of the physical parameters of our system. The precise determination of the equilibrium length is quite difficult due to the complex interactions between the fluid and the grains. However, we can have a crude approximation assuming that the moving grains roll on the sand bed surface and undergo a drag force, $F_d = 0.125 c_d \rho_f \pi d^2 v_r^2$, where v_r is the relative velocity of the grain with respect to that of the fluid, ρ_f is the fluid density and c_d is the drag coefficient which depends on the particle Reynolds number. (c_d will be taken to be equal to $c_d = 24.0/Re_p + 6.0/(1.0 + \sqrt{Re_p}) + 0.4$, [19]). Considering, in addition, that the equilibrium velocity is given, to zero order, by $\gamma d/2$ (where γ is the flow shear rate), ones find:

$$l_{eq} = f(Re_p) \frac{\rho_g}{\rho_f} d, \quad (13)$$

where ρ_g is the grain density and f is a function of the particle Reynolds number $Re_p = \gamma d^2/\nu$. When $Re_p < 1$, $f \simeq 0.035 Re_p$ and for $Re_p > 10^4$, f approaches the constant value 3.3. For intermediate particle Reynolds number (i.e., $1 < Re < 10^3$), the function f can be well fitted by: $f(Re_p) \simeq 0.035 Re_p / (1 + 0.087 Re_p^{0.75})$. The equilibrium length is plotted as a function of Re_p in Figure 2. In water, this length is of order of $d \times f(Re_p)$ since ρ_g and ρ_f are of the same order of magnitude. As a consequence, for small particle Reynolds number (i.e., $Re_p \ll 1$), l_{eq} is much smaller than the particle diameter, which means that l_{eq} can be considered as reduced to zero in the framework of a continuum theory for the description of the granular bed surface.

2.3 Simplification of the problem

We will assume that the typical hydrodynamical time is much smaller than the typical morphological time. In

other words, it means that the flow adapts itself instantaneously to the bed profile. We will therefore solve the stationary version of the hydrodynamical equations for a fixed bed profile. Flow equations reduce then to

$$\rho_f(\mathbf{u} \cdot \nabla)\mathbf{u} = -\nabla p + \eta \nabla^2 \mathbf{u}, \quad (14)$$

$$\nabla \cdot \mathbf{u} = 0, \quad (15)$$

and the boundary conditions at the sand bed surface read

$$-\frac{\partial h}{\partial x} U + V = 0, \quad (16)$$

$$U + \frac{\partial h}{\partial x} V = 0. \quad (17)$$

The evolution equations for the sand bed profile and the sand flux are unchanged and are given by:

$$\frac{\partial q}{\partial x} = -\frac{q - q_{eq}}{l_{eq}}, \quad (18)$$

$$\frac{\partial h}{\partial t} = -\frac{\partial q}{\partial x}, \quad (19)$$

where q_{eq} is given by

$$q_{eq} = q_b \left[\Theta - \frac{\Theta_{c0}}{\sqrt{1 + h_x^2}} \left(1 + \frac{h_x}{\tan \phi_s} \right) \right]^n. \quad (20)$$

In the case where the saturation length l_{eq} goes to zero, we recover the classical expression for the bed profile evolution: $\partial h / \partial t = -\partial q_{eq} / \partial x$.

3 Basic state

The basic state corresponds to the solution of the model equations when the sand bed surface remains flat and horizontal. In that case, the flow velocity profile $U_0(y)$ is given by a simple linear profile:

$$U_0(y) = U_\infty \frac{y}{L} = \gamma y. \quad (21)$$

We recall that γ is the shear rate and L the thickness of the flow.

In the basic state, the flux of transported grains q_0 is easily calculated. It reads:

$$q_0 = q_b(\Theta_0 - \Theta_{c0})^n, \quad (22)$$

where $\Theta_0 = \nu\gamma/g(s-1)d$ is the shield parameter corresponding to a flat sand bed.

4 Linear stability analysis

In order to study the formation of the ripple pattern, we perturb the sand bed so that the profile looks like $h = h_1 e^{ikx + \omega t}$ where h_1 is a small quantity. Note that the wavenumber k characterizes the spacing of the crests and ω denotes the growth rate of the bed pattern. In the following we will use dimensionless variables. We will choose the inverse wavenumber k^{-1} as unit length and the inverse shear rate $\gamma^{-1} = (U_\infty/L)^{-1}$ as unit time.

4.1 Perturbed flow

We will first calculate the flow perturbation, the bed profile being kept fixed. The calculation strategy used here is the same as that exposed in [22]. However, we find it worthwhile to recall the main lines. The perturbed flow quantities can be written as a vector:

$$\begin{pmatrix} U \\ V \\ P \\ h \end{pmatrix} = \begin{pmatrix} U_0(y) \\ 0 \\ P_0 \\ 0 \end{pmatrix} + e^{ikx + \omega t} \begin{pmatrix} U_1(y) \\ V_1(y) \\ P_1(y) \\ h_1 \end{pmatrix}. \quad (23)$$

Note that the subscript 0 refers to the basic solution corresponding to a flat sand bed whereas the subscript 1 denotes perturbed quantities. Plugging equation (23) into the momentum and mass conservation equations (14–15) and keeping only the linear terms, we get:

$$\beta^2 \left(\frac{\partial^2 U_1}{\partial y^2} - U_1 \right) = iyU_1 + V_1 + iP_1, \quad (24)$$

$$\beta^2 \left(\frac{\partial^2 V_1}{\partial y^2} - V_1 \right) = iyV_1 + \frac{\partial P_1}{\partial y}, \quad (25)$$

$$iU_1 + \frac{\partial V_1}{\partial y} = 0, \quad (26)$$

with the following boundary conditions:

$$y = 0 : U_1 = -h_1, V_1 = 0, \quad (27)$$

$$y = \alpha : U_1 = 0, V_1 = 0. \quad (28)$$

We have introduced two dimensionless parameters α and β :

$$\alpha = kL, \quad \beta = k(\nu/\gamma)^{1/2}. \quad (29)$$

β corresponds to a dimensionless viscous length: $\beta = kl_v$ with $l_v = (\nu/\gamma)^{1/2}$.

The exact solution of (24), (25) and (26) can be obtained via the resolution of the equation for the vorticity Ω_1 which reads:

$$\beta^2 \left(\frac{\partial^2 \Omega_1}{\partial y^2} - \Omega_1 \right) = iy\Omega_1, \quad (30)$$

where Ω_1 is defined by $\Omega_1 = \partial_x V_1 - \partial_y U_1$

The solution of equation (30) is a linear combination of Airy functions Ai and Bi :

$$\Omega_1(y) = C_1 Ai(Y) + C_2 Bi(Y), \quad (31)$$

with $Y = e^{i\pi/6}(y - i\beta^2)/\beta^{2/3}$. Then, the stream function ψ_1 (defined as $U_1 = \partial_y \psi_1$ and $V_1 = -\partial_x \psi_1$) can be obtained from the equation:

$$\partial_y^2 \psi_1 - \psi_1 = -\Omega_1, \quad (32)$$

whose solution is

$$\psi_1(y) = \frac{1}{2} \left\{ e^{-y} \int_0^y d\xi \Omega_1(\xi) e^\xi - e^y \int_0^y d\xi \Omega_1(\xi) e^{-\xi} \right\} + C_3 e^{-y} + C_4 e^y. \quad (33)$$

The constant C_1 , C_2 , C_3 and C_4 are determined by the boundary conditions (27–28) (see Appendix).

As stated previously, we assume that the flow thickness L is much larger than the characteristic length scales of the sand bed deformation. In particular, L is assumed to be much larger than the wavelength of the sand pattern, so that $\alpha = kL \gg 1$. In this limit, the stream function takes the following simple form:

$$\psi_1(y) = -h_1 \left\{ e^{-y} \int_0^y d\xi Ai(\xi') e^\xi - e^y \int_0^y d\xi Ai(\xi') e^{-\xi} \right\} / \left\{ 2 \int_0^\infty d\xi e^{-\xi} Ai(\xi') \right\} - h_1 \sinh(y), \quad (34)$$

where $\xi' = e^{i\pi/6}(\xi - i\beta^2)/\beta^{2/3}$. The perturbed bed shear stress σ_{1b} can then be easily calculated:

$$\frac{\sigma_{1b}}{\eta\gamma} = \frac{\partial^2 \psi_1}{\partial y^2}(y=0) = \frac{h_1 Ai(-ie^{i\pi/6}\beta^{4/3})}{\int_0^\infty e^{-\xi} Ai(\xi') d\xi}. \quad (35)$$

We can derive an approximate analytical expression for σ_1 in two limit cases: (i) when the wavelength of the bed profile is much larger than the viscous length l_v (i.e., $\beta \ll 1$) and (ii) when it is much smaller than l_v (i.e., $\beta \gg 1$). For $\beta \ll 1$, we get:

$$\frac{\sigma_{1b}}{\eta\gamma} = \frac{h_1}{l_v} \left[1.06 e^{i\pi/6} \beta^{1/3} + 0.83 \beta + 0.43 e^{i\pi/3} \beta^{5/3} + O(\beta^{7/3}) \right], \quad (36)$$

and for $\beta \gg 1$, we obtain:

$$\frac{\sigma_{1b}}{\eta\gamma} = \frac{h_1}{l_v} \left[2\beta + \frac{i}{2\beta} + O\left(\frac{1}{\beta^3}\right) \right]. \quad (37)$$

In Figure 3, we have plotted the real and imaginary part of the perturbed bed shear stress. We can note that it exhibits a positive phase lag ψ [$\psi = \text{Re}(\sigma_{1b})/\text{Im}(\sigma_{1b})$] with respect to the bed perturbation due to the existence of a non zero imaginary part. As explained in the introduction, this phase lag will be responsible for the bed instability. For short wavelength perturbation, the phase lag vanishes to zero.

4.2 Growth rate and drift velocity

We are now in position to calculate the growth rate ω of the bed profile perturbation. The linearization of the equilibrium sediment flux expression [see Eq. (20)] gives:

$$q_{eq} = q_{eq}^{(0)} + q_{eq}^{(1)} \quad (38)$$

with

$$q_{eq}^{(1)} = n q_b \Theta_{c0}^n \mu^{n-1} \left[\frac{\Theta_1}{\Theta_{c0}} - \frac{h_{1x}}{\tan \phi_s} \right], \quad (39)$$

We set $\mu = (\Theta_0 - \Theta_{c0})/\Theta_{c0}$. The parameter μ measures the distance from the threshold of grain motion and will

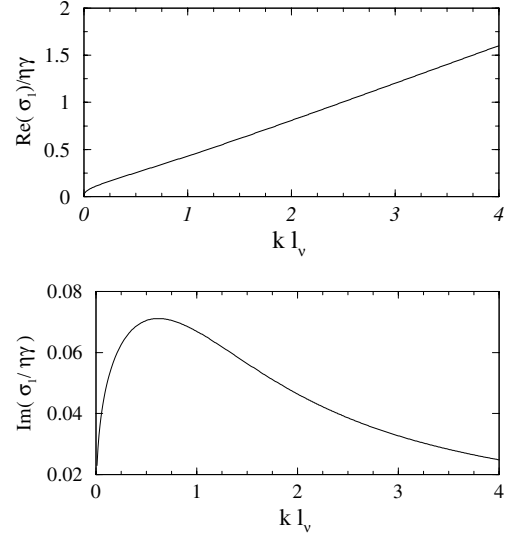


Fig. 3. Real and imaginary parts of the perturbed bed shear stress calculated from the exact expression. $h_1/l_v = 0.2$.

be referred to as the relative shear stress excess. The first term in equation (39) encodes the hydrodynamical drag while the second one describes the bed slope effect (or gravity effect) on the sediment transport.

Linearizing the equations governing the sediment transport [Eqs. (19–18)] and using equation (39), we get a close expression for the growth rate of the perturbation of wave number k :

$$\omega = n q_b \Theta_{c0}^n \mu^{n-1} \left[-i \frac{\Theta_1}{\Theta_{c0}} \frac{k}{h_1} - \frac{k^2}{\tan \phi_s} \right] \times \frac{(1 - ikl_{eq})}{(1 + k^2 l_{eq}^2)}. \quad (40)$$

The above expression for the growth rate is only valid for $\mu > 0$.

In order to identify the physical mechanisms responsible for the ripple instability, we will treat different limiting cases according to the values of the parameters ϕ_s (the intern angle of friction of the granular material) and l_{eq} (the equilibrium length), before we handle the general situation.

4.2.1 Case: No gravity and no inertia

In case where gravity and grain inertia are ignored (i.e., $\phi_s = \pi/2$ and $l_{eq} = 0$), we find that the growth rate is given in the long wavelength limit (i.e., $\beta \ll 1$) by

$$\text{Re}(\omega) = \frac{d^2}{l_v^2} \omega_0 \mu^{m-1} (1 + \mu) \left[0.53 \beta^{4/3} + O(\beta^{8/3}) \right], \quad (41)$$

$$\text{Im}(\omega) = -\frac{d^2}{l_v^2} \omega_0 \mu^{n-1} (1 + \mu) \left[0.92 \beta^{4/3} + O(\beta^2) \right], \quad (42)$$

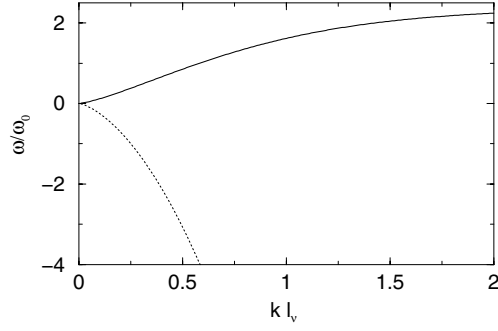


Fig. 4. Real (continuous line) and imaginary part (dash line) of the growth rate in the case where bed slope and grain inertia effects are ignored. $\mu = 0.1$, $\nu = 10^{-6}$ m²/s and $d = 100$ μ m.

whereas for large β , we obtain to dominant order:

$$\text{Re}(\omega) = 0.5 \frac{d^2}{l_\nu^2} \omega_0 \mu^{n-1} (1 + \mu), \quad (43)$$

$$\text{Im}(\omega) = -2 \frac{d^2}{l_\nu^2} \omega_0 \mu^{n-1} (1 + \mu) \beta^2. \quad (44)$$

We set $\omega_0 = n(q_b/d^2)\Theta_{c0}^n$. These results are illustrated in Figure 4. A positive growth rate indicates an unstable mode. We can see that the real part of ω is positive whatever the value of k : it grows first as $k^{4/3}$ and saturates to a finite value at large k . Such an analysis predicts therefore that all waves grow and furthermore the shorter the wave the faster the growth. As a first conclusion, the properties of the viscous flow leads to a sand bed instability, generated by the phase lag between the bed shear stress and the bed perturbation which is due to fluid inertia. Secondly, according to the present analysis, the shortest waves should dominate which is obviously unrealistic. To circumvent this problem and to damp the growth of the short waves, both neglected effects (i.e., gravity and grain inertia) should be considered.

4.2.2 Case: Gravity and no inertia

We first introduce the bed slope effect on sediment transport (i.e., $\phi_s \neq \pi/2$), still neglecting grain inertia. In this situation and in the long wavelength limit, the growth rate reads:

$$\text{Re}(\omega) = \frac{d^2}{l_\nu^2} \omega_0 \mu^{n-1} \left[0.53 (1 + \mu) \beta^{4/3} - \frac{\beta^2}{\tan \phi_s} \right], \quad (45)$$

$$\text{Im}(\omega) = -0.92 \frac{d^2}{l_\nu^2} \omega_0 \mu^{n-1} (1 + \mu) \beta^{4/3}. \quad (46)$$

The variation of the growth rate as a function of the relative shear stress excess μ is shown in Figure 5. One can note that the bed slope effect [corresponding to the term proportional to k^2 in Eq. (45)] acts as a stabilizing mechanism: it damps the short waves. As a consequence, a fastest growing wave appears. Its order of magnitude is

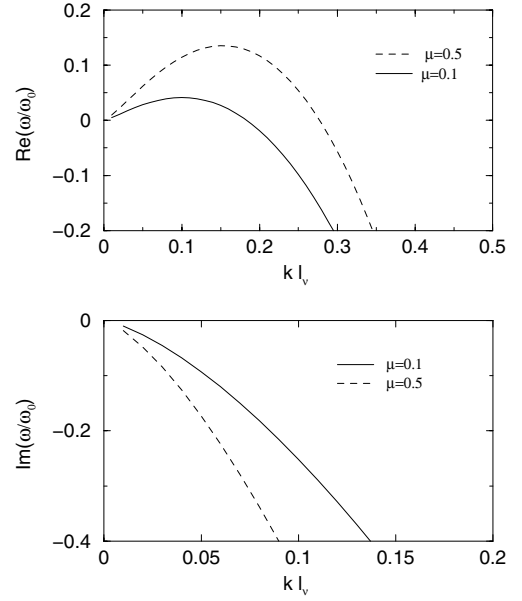


Fig. 5. Real and imaginary parts of the growth rate for $\mu = 0.1$ and $\mu = 0.5$ in the case where grain inertia effect is ignored. $\phi_s = 30^\circ$, $\Theta_{c0} = 0.2$, $s = 2.7$ $\nu = 10^{-6}$ m²/s, and $d = 100$ μ m.

given by the balance of the hydrodynamical term and the gravity one in equation (45). One gets:

$$\lambda_{max} = \frac{2\pi}{k_{max}} \simeq \frac{30 l_\nu}{(\tan \phi_s)^{3/2} (1 + \mu)^{3/2}}. \quad (47)$$

In the latter expression, we should be aware of that the viscous length $l_\nu = \sqrt{\nu/\gamma}$ and μ are not independent variables. We recall that μ measures the distance from the grain motion threshold: $\mu = \gamma\nu/g(s-1)d\Theta_{c0} - 1$. It follows that given the grain density ρ_g , the grain diameter d and the fluid viscosity ν , choosing a value for μ amounts to fix the shear rate γ . Expressing γ as a function of μ , the expression for the most dangerous wavelength can be rewritten as:

$$\lambda_{max} = \frac{30}{\Theta_{c0}^{1/2} (\tan \phi_s)^{3/2}} \frac{\nu}{\sqrt{g(s-1)d} (1 + \mu)^2}. \quad (48)$$

The evolution of λ_{max} as function of μ is shown in Figure 6. It decreases as the relative shear stress excess μ increases and as the grain diameter gets larger. In the case of sand grains in a water flow (i.e., $\nu = 10^{-6}$ m²/s, $s = 2.7$ and $\phi_s = 30^\circ$), we obtain $\lambda_{max} \simeq 0.5$ cm for $d = 50$ μ m and $\mu = 0.1$. From the analytical expression (48), one can deduce scaling laws for λ_{max} as a function of the physical parameters of the system. In particular, close to the grain motion threshold (i.e., $\mu \ll 1$), the most dangerous mode scales as $\lambda_{max} \sim \nu/\sqrt{g(s-1)d}$.

We can also evaluate the growth rate of the most dangerous mode (see Tab. 1). In the long wavelength limit and close to the grain motion threshold, the growth rate increases with the grain diameter and the shear stress excess and decreases with the fluid viscosity.

It is also important to note that the granular bed is always unstable as soon as $\mu > 0$ (i.e., as soon as the grain

Table 1. Expressions for the wavelength, the growth rate and the drift velocity of the most dangerous mode at small and large μ in the case where grain inertia is ignored. $A = n c$. We recall that n is the exponent of the transport law and c a numerical constant appearing in the expression of q_b .

	$\mu \ll 1$	$\mu \gg 1$
λ_{max}	$30. \Theta_{c0}^{-1/2} (\tan \phi_s)^{-3/2} \frac{\nu}{\sqrt{g(s-1)d}}$	$18. \Theta_{c0}^{-1/2} (\tan \phi_s)^{-1/2} \frac{\nu}{\mu \sqrt{(s-1)gd}}$
ω_{max}	$0.02 A (\tan \phi_s)^2 \Theta_{c0}^{n+1} \mu^{n-1} \frac{(s-1)^{3/2} g^{3/2} d^{5/2}}{\nu^2}$	$0.375 A \Theta_{c0}^{n+1} \mu^{n+1} \frac{(s-1)^{3/2} g^{3/2} d^{5/2}}{\nu^2}$
v_d	$0.53 A (\tan \phi_s)^{1/2} \Theta_{c0}^{n+1/2} \mu^{n-1} \frac{(s-1) g d^2}{\nu}$	$A (\tan \phi_s)^{1/2} \Theta_{c0}^{n+1/2} \mu^{n+1} \frac{(s-1) g d^2}{\nu}$

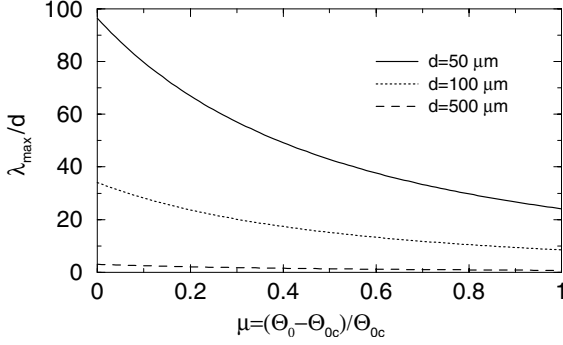


Fig. 6. Evolution of the most dangerous mode λ_{max} as a function of μ for different grain diameters in the case where grain inertia effect is ignored. $\phi_s = 30^\circ$, $\Theta_{c0} = 0.2$, $s = 2.7$ and $\nu = 10^{-6} \text{ m}^2/\text{s}$.

motion becomes possible). Furthermore, all the unstable mode have a growth rate with a negative imaginary part (see Fig. 5), which means that unstable waves drift along the sand surface in the direction of the flow. The larger the wave is, the lower the drift velocity is. The drift velocity V_d of the unstable mode can be easily estimated ($V_d = -Im(\omega)/k$) and is given in Table 1.

Finally, one should note that the above scaling laws for the wavelength of the most dangerous and its growth rate, as well as for the drift velocity of the unstable modes, have been derived in the long wavelength limit (i.e., $\beta = kl_\nu \ll 1$). This limit is justified as soon as one remains close to the grain motion threshold. Far from it (i.e., $\mu \gg 1$), the expression derived for the most dangerous mode [Eq. (47)] is no longer valid since β_{max} becomes greater than one. However, it is still possible to calculate the growth rate in the short wavelength limit and deduce the expression for the most dangerous mode in this limit. We obtain: $\lambda_{max} \sim \sqrt{gd}/\gamma$. The most dangerous mode in this limit is therefore inversely proportional to the shear rate and is independent of the fluid viscosity.

4.2.3 Case: No gravity and grain inertia

We neglect here the bed slope effect on the sediment transport but we include the grain inertia effect which is expected to be pertinent when Re_p is larger than unity as to be seen later on. In this case and in the long wavelength

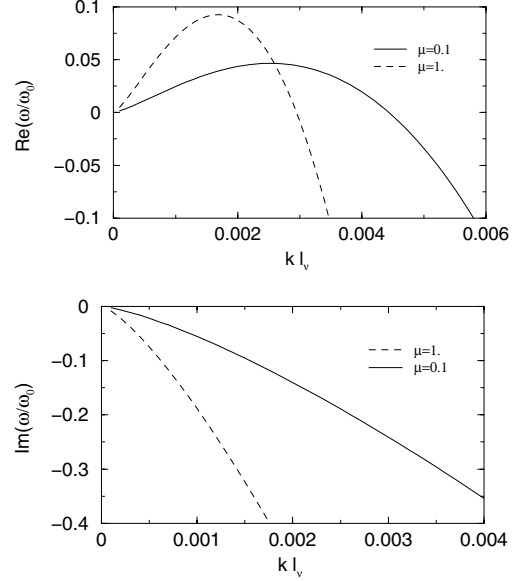


Fig. 7. Real and imaginary parts of the growth rate for $\mu = 0.1$ and $\mu = 1$, in the case where bed slope effect is ignored. $\Theta_{c0} = 0.2$, $s = 2.7$, $\nu = 10^{-6} \text{ m}^2/\text{s}$, and $d = 500 \text{ }\mu\text{m}$.

limit the growth rate reads:

$$\text{Re}(\omega) = \frac{d^2}{l_\nu^2} \omega_0 \mu^{n-1} (1 + \mu) \times \left[0.53 \beta^{4/3} \left(1 - \sqrt{3} \frac{l_{eq}}{l_\nu} \beta \right) \right], \quad (49)$$

$$\text{Im}(\omega) = -0.92 \frac{d^2}{l_\nu^2} \omega_0 \mu^{n-1} (1 + \mu) \beta^{4/3}. \quad (50)$$

The grain inertia effect plays a stabilizing role for short waves and scales as $\beta^{7/3}$ (or $k^{7/3}$). As a consequence, there exists a band of unstable modes (see Fig. 7) where the most dangerous one, β_{max} , is given by:

$$\beta_{max} = 0.33 \frac{l_\nu}{l_{eq}}, \quad (51)$$

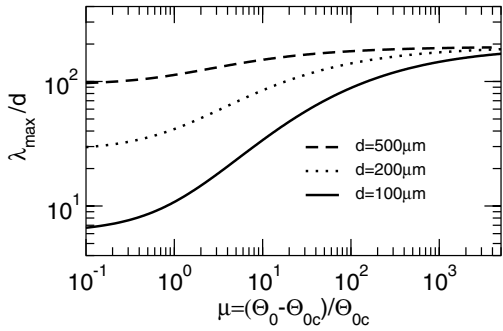
which yields

$$\lambda_{max} = 3.5 \pi \sqrt{3} l_{eq} = 3.5 \pi \sqrt{3} f(Re_p) \frac{\rho_g}{\rho_f} d. \quad (52)$$

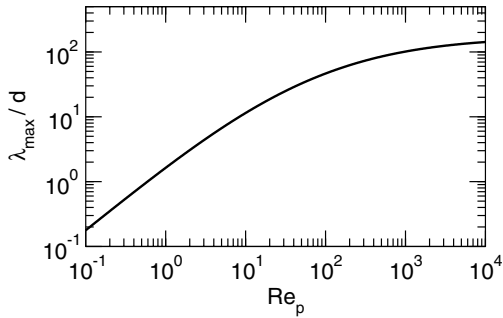
This expression has been derived in the long wavelength limit where $\beta \ll 1$ and is therefore valid as soon as $l_{eq} > l_\nu$ or equivalently when the particle Reynolds number is greater than unity. The evolution of λ_{max} as a function of the relative shear stress excess μ for different grain

Table 2. Expressions for the wavelength, the growth rate and the drift velocity of the most dangerous mode in the case where gravity is ignored. $Re_p = \gamma d^2/\nu$, $Re_{p0} = (s-1)gd^3\Theta_{c0}/\nu^2$ and $A = nc$. Re_{p0} is the value of the particle Reynolds number at the onset of grain motion. We recall that n is the exponent of the transport law and c is a numerical constant appearing in the expression of q_b .

	$Re_p < 1$	$1 < Re_p < 10^3$
λ_{max}	$0.66 Re_p s d$	$0.66 \frac{Re_p}{1+0.087 Re_p^{0.75}} s d$
ω_{max}	$9. A \Theta_{c0}^n \frac{(s-1)^{1/2}}{s^{4/3}} \sqrt{\frac{g}{d}} \frac{(Re_p - Re_{p0})^{n-1}}{(Re_{p0})^n}$	$9. A \Theta_{c0}^n \frac{(s-1)^{1/2}}{s^{4/3}} \sqrt{\frac{g}{d}} \frac{(Re_p - Re_{p0})^{n-1}}{(Re_{p0})^n} (1 + 0.087 Re_p^{0.75})^{4/3}$
v_d	$0.725 A. \Theta_{c0}^n \frac{(s-1)^{1/2}}{s^{1/3}} \sqrt{gd} \frac{(Re_p - Re_{p0})^{n-1}}{(Re_{p0})^{n-1}}$	$0.725 A. \Theta_{c0}^n \frac{(s-1)^{1/2}}{s^{1/3}} \sqrt{gd} \frac{(Re_p - Re_{p0})^{n-1}}{(Re_{p0})^{n-1}} (1 + 0.087 Re_p^{0.75})^{1/3}$



(a)



(b)

Fig. 8. Evaluation of the most dangerous mode λ_{max} in the case where the bed slope effect is ignored. (a) λ_{max} versus the relative shear stress excess μ for different grain diameters, (b) λ_{max} versus the particle Reynolds number. Parameters: $\Theta_{c0} = 0.2$, $s = 2.7$ and $\nu = 10^{-6} \text{ m}^2/\text{s}$.

diameters is shown in Figure 8. Contrary to the previous situation, the wavelength of the most dangerous mode increases as the relative shear stress excess increases and as the grain diameter gets bigger. Furthermore, λ_{max} saturates at high values of the shear stress excess μ . In the case of sand grains in a water flow (i.e., $\nu = 10^{-6} \text{ m}^2/\text{s}$ and $s = 2.7$), we get $\lambda_{max} \simeq 6 \text{ cm}$ for $d = 500 \text{ }\mu\text{m}$ and $\mu = 0.1$.

At small particle Reynolds number (i.e., $Re_p < 1$), we have seen that $f(Re_p) \sim Re_p$ so that the expression for the most unstable wavelength reduces to:

$$\lambda_{max} \simeq 0.66 \frac{\rho_g}{\rho_f} Re_p d. \quad (53)$$

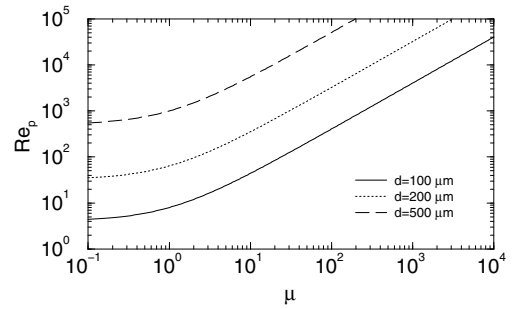


Fig. 9. Correspondence between the particle Reynolds number and the relative shear stress excess μ for different grain diameters ($Re_p = (s-1)gd^3\Theta_{c0}(1+\mu)/\nu^2$). $\Theta_{c0} = 0.2$, $s = 2.7$ and $\nu = 10^{-6} \text{ m}^2/\text{s}$.

This regime of small particle Reynolds number is encountered in the case where the grain diameter is small enough (i.e., $d \leq 100 \text{ }\mu\text{m}$) and the shear stress close enough to the grain motion threshold (see Fig. 9). The growth rate and phase velocity associated with the most dangerous mode is given in Table 2.

At intermediate particle Reynolds number (i.e., $10^3 > Re_p > 1$), we obtain different scalings since $f(Re_p)$ does not vary any more linearly with Re_p . This regime is reached for sufficiently large values of the shear stress excess μ or large values of the grain diameter (see Fig. 9). In this regime, the wavelength of the most dangerous mode scales as:

$$\lambda_{max} \simeq 0.66 \frac{\rho_g}{\rho_f} \frac{Re_p}{1 + 0.087 Re_p^{0.75}} d. \quad (54)$$

The growth rate and phase velocity associated with this mode are given in Table 2.

Finally, one should point out that at very large particle Reynolds number (i.e., $Re_p > 1000$), one could expect that the flow be turbulent and that our laminar analysis should therefore break down. A flow between two plates becomes turbulent when the flow Reynolds number is greater than 1000. We recall that the flow Reynolds number is based on a length scale related to the height or width of the flow and is therefore greater than the corresponding particle Reynolds number. As a consequence, flows are expected to become turbulent for particle Reynolds much smaller than 1000, except for quasi-2D flows (i.e., in Hele-Shaw cell with a gap of order of the grain size), for

which the flow Reynolds number is of the same order as the particle Reynolds number.

4.2.4 General case: Gravity and inertia

At last, we analyze the general situation where both stabilizing effects (gravity and grain inertia) are taken into account and determine when one prevails over the other. In the general case, at small β the growth rate reads:

$$\text{Re}(\omega) = \frac{d^2}{l_v^2} \omega_0 \mu^{n-1} \times 0.53 (1 + \mu) \beta^{4/3} \times \left(1 - \frac{\beta^{2/3}}{0.53 \tan \phi_s (1 + \mu)} - \sqrt{3} \frac{l_{eq}}{l_v} \beta \right), \quad (55)$$

$$\text{Im}(\omega) = -0.92 \frac{d^2}{l_v^2} \omega_0 \mu^{n-1} (1 + \mu) \beta^{4/3}. \quad (56)$$

One can note in expression (55) the presence of the two terms associated with the gravity and grain inertia effects which scale respectively as β^2 and $\beta^{7/3}$. One expects therefore that gravity effect should prevail for long wavelength modes and grain inertia should dominate for modes of smaller wavelengths. The general expression of the most dangerous mode can be estimated by determining the extremum of expression (55). It yields:

$$\lambda_{max} = 1.75\pi \sqrt{3} l_{eq} \left[(1 + \sqrt{1-r})^{1/3} + (1 - \sqrt{1-r})^{1/3} \right]^3, \quad (57)$$

where r measures the magnitude of the gravity effect with respect to that of the grain inertia one and is given by:

$$r = \frac{8}{147} \frac{l_v^2}{(0.53 \tan \phi_s)^3 (1 + \mu)^3 l_{eq}^2}. \quad (58)$$

When $r \gg 1$, we recover that $\lambda_{max} \sim l_v / (1 + \mu)^{3/2}$ [cf. Eq. (47)], and whereas for $r \ll 1$, we get $\lambda_{max} = 3.5\pi \sqrt{3} l_{eq}$ [cf. Eq. (52)]. The critical situation where both gravity and grain inertia effects are of the same order of magnitude corresponds to $r_c = 1$. This critical condition can be expressed in terms of a critical particle Reynolds number Re_{pc} which is found to depend on the Galileo number Ga defined as $Ga = (s-1)gd^3/\nu^2$. The critical particle Reynolds number Re_{pc} as a function of Ga is shown in Figure 10. When $Re_p > Re_{pc}$, inertia effects prevails whereas gravity effect becomes dominant for $Re_p < Re_{pc}$. At low particle Reynolds number (i.e., $Re_p < 1$), it is found that $Re_{pc} \sim (Ga^3 \Theta_{c0}^3 / s^2 \tan \phi_s)^{1/6}$, while at high particle Reynolds number $Re_{pc} \sim (Ga^3 \Theta_{c0}^3 / s^2 \tan \phi_s)^{1/4}$. As an example, for water flows, we obtain that $Re_{pc} \approx 2$ for sand grains of diameter $d = 50 \mu\text{m}$ whereas $Re_{pc} \approx 80$ for $d = 500 \mu\text{m}$.

The variation of λ_{max} as a function of the particle Reynolds number is shown in Figure 11 for different grain diameters. One can clearly see the two regimes, one at low particle Reynolds number dominated by gravity effect and

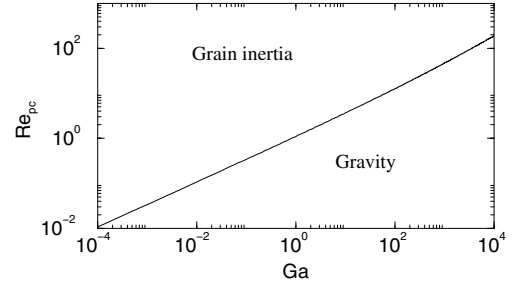


Fig. 10. Critical particle number Re_{pc} as a function of the Galileo number. Above the curve, inertia effects prevails whereas above it gravity effect becomes dominant. $\Theta_{c0} = 0.2$, $\phi_s = 30^\circ$ and $s = 2.7$. For water flows, the Galileo number is equal to $Ga = 2.5, 20, 160, 2500$ respectively for grains of diameter $d = 50, 100, 200, 500 \mu\text{m}$.

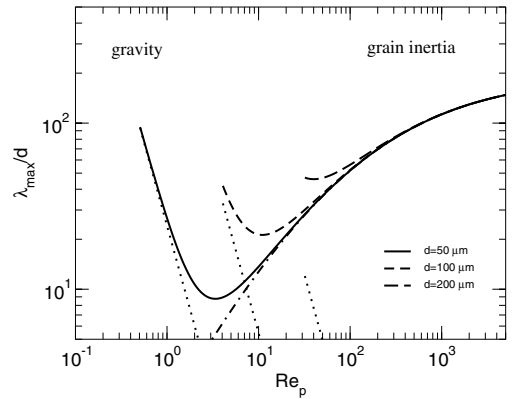


Fig. 11. Evolution of λ_{max} as a function of the particle Reynolds number Re_p for different grain diameters. At small particle Reynolds number, the gravity effect is dominant, while at large Re_p grain inertia effect prevails. The dotted curves (respectively dot-dashed lines) corresponds to the most dangerous mode in absence of grain inertia (resp. in absence of gravity effect). $\phi_s = 30^\circ$, $s = 2.7$ and $\nu = 10^{-6} \text{m}^2/\text{s}$.

the other at large particle Reynolds number governed by the grain inertia effect. One can note also that the regime where gravity effect prevails shrinks as the grain diameter increases.

As a conclusion, the main result of this analysis can be stated as follows: at small particle Reynolds number, the most dangerous mode is driven by the gravity effect whereas at larger Re_p , it is governed by grain inertia. For intermediate particle Reynolds number, there exists a cross-over regime, where the most dangerous mode is a non-trivial combination of the viscous length and the equilibrium length given by expression (57).

5 Discussion and conclusion

5.1 Discussion

In this article, we have presented an analytical model for the instability of a sand bed sheared by a laminar shear flow. We find that the sand bed is unstable as soon as

the flow is capable of carrying sand grains. The instability results from the competition between a destabilizing mechanism due to fluid inertia and a stabilizing effect whose origin is different depending on the value of the particle Reynolds number. At low particle Reynolds number, bed slope effect prevails whereas at large particle Reynolds number, the stabilizing mechanism is due to grain inertia. It is found that at small particle Reynolds number, the wavelength of the most dangerous mode scales as the viscous length $l_\nu = (\nu/\gamma)^{1/2}$ and varies as the equilibrium length associated with the grain inertia, $l_{eq} = f(Re_p) (\rho_g/\rho_f) d$, for larger particle Reynolds number. For intermediate particle Reynolds number, there exists a cross over regime, where the wavelength of the most amplified mode is a complex combination of the viscous length l_ν and the equilibrium length l_{eq} . In addition, we derived analytical expressions for the wave velocity and growth rate of the unstable mode in these different regimes.

The natural question which arises is the pertinence of the model and its agreement with the experiments. First, our predictions are expected to describe correctly the growth of the ripple pattern only in the first stages of the instability, before nonlinear effects come into play. Second, it turns out that most of experiments on ripple formation have been achieved in turbulent flows and there are only few data available in the literature about laminar flow experiments. Recent careful studies on the onset of sand ripple formation have been performed by the Bayreuth group [23,24], but unfortunately they pertain to turbulent flow situations. The flow Reynolds number in those experiments is of order of 10^6 . As far as we know, there is only one group investigating ripple formation in a laminar flow configuration: this is the Orsay group [13]. They study the ripple formation process in a Hele-Shaw cell (i.e., in a quasi-2D configuration) where laminar flow conditions are fulfilled. They have not yet accumulated extensive data to allow a thorough confrontation with our predictions but preliminary comparisons can be made. Taking their experimental parameters corresponding to a regime where grain inertia is pertinent ($Re_p \approx 100$ and $d = 200 \mu$) [13], the estimation of the most dangerous mode drawn from our predictions (i.e., from $\lambda_{max} = 3.5\pi\sqrt{3}l_{eq}$), gives a few centimeters, which seems compatible with the measured ripple wavelength at the first stages of the instability. On the other hand, in the regime where grain inertia becomes negligible, our prediction underestimates the ripple wavelength by a least of factor of 10. We are looking forward, in the near future, to make more conclusive comparisons concerning the scaling laws for the wavelength and drift velocity of the ripple pattern as a function of the shear rate, grain diameter and fluid viscosity.

5.2 Conclusion

The aim of the present study was to improve the understanding of ripple formation in laminar shear flows. We have proposed a model where we have taken into account

bed slope and grain inertia effects in the sediment transport. Within this model, we have derived analytical expressions of the wavelength of the most dangerous mode, as well as the growth rate and wave velocity of the unstable modes against all parameters. Unfortunately, extensive experimental data in laminar regime are still lacking. There is therefore a strong need of well-controlled and well-designed experiments where the growth of the ripples is investigated in laminar flow configurations.

Parallel to this, the model used here can be refined by including a stronger coupling between the fluid flow and the bed. The present model accounts for this coupling only via the particle transport rate. It may be interesting to investigate the feedback mechanism between the presence of sand grains in the fluid and the fluid flow. Another important issue should be treated, that is the nonlinear development of the ripple structure. In particular, it is known that the ripple structure undergoes a coarsening process in which the ripple wavelength increases in course of time and it is still not clear whether this coarsening interrupts or not at long time. To understand the long-time behavior of the ripples and the coarsening process, a non-linear analysis based on sound modeling is strongly needed. It would be, for example, important to determine for which conditions one can observe the interruption of the coarsening process and what are the underlying non-linear mechanisms.

A. Valance is grateful to C. Misbah for numerous and stimulating discussions about sand transport modeling.

Appendix

The integration constant in equation (33) are given by:

$$C_1 = h_1 \frac{B^- - B^+}{A^- B^+ - A^+ B^-} \quad (59)$$

$$C_2 = h_1 \frac{A^+ - A^-}{A^- B^+ - A^+ B^-} \quad (60)$$

$$C_3 = -\frac{h_1}{2} \quad (61)$$

$$C_4 = \frac{h_1}{2} \quad (62)$$

with

$$A^\pm = \int_0^\alpha dy Ai(Y) e^{\pm y} \quad (63)$$

$$B^\pm = \int_0^\alpha dy Bi(Y) e^{\pm y}. \quad (64)$$

Ai and Bi are Airy functions of first and second species.

References

1. J. Fredsoe, R. Deigaard, *Mechanics of Coastal Sediment Transport* (World Scientific, 1992)
2. J.F. Kennedy, *J. Fluid Mech.* **16**, 521 (1963)

3. J.F. Kennedy, *Ann. Rev. Fluid Mech.* **1**, 147 (1969)
4. M.H. Gradowczyk, *J. Fluid Mech.* **33**, 93 (1968)
5. S.E. Coleman, J.D. Fenton, *J. Fluid Mech.* **418**, 101 (2000)
6. K.J. Richards, *J. Fluid Mech.* **99**, 597 (1980)
7. B.M. Sumer, M. Bakioglu, *J. Fluid Mech.* **144**, 117 (1984)
8. J. Nikuradse, *V.D.I.-Forschungheft*, no. 361 (1933)
9. J.D. Smith, S.R. McLean, *J. Geophys. Res.* **82**, 1735 (1977)
10. S.E. Coleman, B.W. Melville, *J. Hydr. Engng. ASCE* **122**, 301 (1996)
11. M.S. Yalin, *J. Hydr. Engng. ASCE* **111**, 1148 (1985)
12. F. Charru, H. Mouilleron-Arnould, *J. Fluid Mech.* **452**, 303 (2002)
13. T. Loiseleux, D. Doppler, P. Gondret, J.-M. Rabaud, in *Second Intertational Workshop on Marine Sandwave and River Dynamics*, edited by J.M.H. Hulscher, T. Garlan, D. Idier (University of Twente, Enschede 2004), pp. 200
14. G. Sauer mann, K. Kroy, H.J. Herrmann, *Phys. Rev. E* **64**, 031305 (2001)
15. B. Andreotti, P. Claudin, S. Douady, *Eur. Phys. J. B* **28**, 341 (2002)
16. P. Hersen, *Eur. Phys. J. B.* **37**, 507 (2004)
17. J.-P. Bouchaud, M.E. Cates, R. Prakash, S.F. Edwards, *Phys. Rev. Lett.* **74**, 1982 (1995)
18. A. Valance, unpublished (2004)
19. F. White, *Viscous Fluid Flow*, McGraw-Hill (New-York, 1974)
20. P. Mantz, *Sedimentology* **25**, 83 (1977)
21. R.A. Bagnold, *Phil. Trans. R. Soc. Lond. A* **249**, 235 (1956)
22. F. Charru, E.J. Hinch, *J. Fluid Mech.* **414**, 195 (2000)
23. A. Betat, V. Frette, I. Rehberg, *Phys. Rev. Lett.* **83**, 88 (1999)
24. A. Betat, C.A. Kruelle, V. Frette, I. Rehberg, *Eur. Phys. J. E* **8**, 465 (2002)